Additive Manufacturing 25 (2019) 399–411

Contents lists available at ScienceDirect

Additive Manufacturing

journal homepage: www.elsevier.com/locate/addma

Computational mechanical characterization of geometrically transformed Schwarz P lattice tissue scaffolds fabricated via two photon polymerization (2PP)

Adi Z. Zabidi[a,*], Shuguang Li[b], Reda M. Felfel[a,d], Kathryn G. Thomas[a], David M. Grant[a], Donal McNally[c], Colin Scotchford[a]

[a] Advanced Materials Research Group, Faculty of Engineering, University of Nottingham, United Kingdom
[b] Composites Research Group, Faculty of Engineering, University of Nottingham, United Kingdom
[c] Bioengineering Research Group, Faculty of Engineering, University of Nottingham, United Kingdom
[d] Physics Department, Faculty of Science, Mansoura University, Mansoura, Egypt

ARTICLE INFO

Keywords:
Tissue scaffold
Schwarz P TPMS structure
Two-photon polymerization (2PP)
Micromechanical analysis
Beam bending
Column buckling

ABSTRACT

Schwarz P unit cell-based tissue scaffolds comprised of poly(D,L-lactide-co-ε-caprolactone)(PLCL) fabricated via the additive manufacturing technique, two-photon polymerisation (2PP) were found to undergo geometrical transformations from the original input design. A Schwarz P unit cell surface geometry CAD model was reconstructed to take into account the geometrical transformations through CAD modeling techniques using measurements obtained from an image-based averaging technique before its implementation for micromechanical analysis. Effective modulus results obtained from computational mechanical characterization via micromechanical analysis of the reconstructed unit cell assigned with the same material model making up the fabricated scaffolds demonstrated excellent agreement with a small margin of error at 6.94% from the experimental mean modulus (0.69 ± 0.29 MPa). The possible sources for the occurrence of geometrical transformations are discussed in this paper. The inter-relationships between different dimensional parameters making up the Schwarz P architecture and resulting effective modulus are also assessed and discussed. With the ability to accommodate the geometrical transformations, maintain efficiency in terms of time and computational resources, micromechanical analysis has the potential to be implemented in tissue scaffolds with a periodic microstructure as well as other structures outside the field of tissue engineering in general.

1. Introduction

Technological advancements over recent years have enabled the implementation of computer aided design (CAD) beyond conventional applications demonstrated in automotive, civil and aeronautical engineering. With developments in imaging technologies as well as reverse engineering techniques, CAD can now be implemented in the realms of biomedical engineering with applications in clinical medicine through to the manufacturing of patient specific customized implants in a new field known as computer aided tissue engineering (CATE) [1]. Implementation of CAD in CATE reduces experimental testing stages and shortens the duration of the tissue scaffold design process through the use of computer techniques based on mechanical design [2]. By pairing the above with additive manufacturing techniques, tissue scaffolds can be easily fabricated and reproduced while also allowing precise control over scaffold micro-structural parameters such as pore size, shape and interconnectivity [3].

The implementation of two-photon polymerization (2PP) has been widespread with applications found in photonic crystals, microfluidic devices, biomedical science, micro-optics, dielectrics and metamaterials [4]. Unlike traditional 3D prototyping techniques such as stereolithography, inkjet printing and laser sintering, 2PP is able to fabricate 3-dimensional structures with feature sizes smaller than the diffraction limit of an applied laser length at submicron resolutions [5–7]. Femtosecond lasers used has been reported to be powerful for advanced materials processing at a micro- and nano- scale level compared to traditional laser processing techniques with its attribution of ultrashort pulse widths and extremely high peak intensities [8]. Through 2PP, CAD model files can be directly transferred to the structure in its physical form out of photopolymer in tens of minutes. The whole

* Corresponding author.
E-mail address: eaxaz@nottingham.ac.uk (A.Z. Zabidi).

https://doi.org/10.1016/j.addma.2018.11.021
Received 14 September 2018; Received in revised form 6 November 2018; Accepted 17 November 2018
Available online 22 November 2018

fabrication process of a structure consists of a few steps and can be performed under one hour. Both processes mentioned can be repeated immediately as required and/or if parameters of the structure require modifications before undergoing the fabrication process again thus demonstrating the repeatability and reproducibility of 2PP [9]

The need for experimental evaluation of mechanical and/or biological responses can be reduced by implementing mathematical models. The mathematical models can be implemented in the form of finite element simulations with tissue scaffold CAD models which thus enabled studies to evaluate their mechanical properties and biomimetic properties [2,10]. One such model, micromechanical analysis involves reducing a tissue scaffold consisting of periodic microstructures to a representative unit cell through derivations of boundary conditions made based on geometrical symmetries.

Triply periodic minimal surfaces (TPMS) topologies have found a place in various applications such as heat transfer, fluid permeability and acoustic attenuation [11–13]. The architecture of TPMS surfaces exhibit properties which make them ideal in systems that can be improved upon through the implementation of fluid dynamics [14]. In the field of tissue engineering, TPMS has particularly been implemented in applications for the design of biomorphic scaffolds due to their smoothly curved surfaces which provide a feasible environment for recuperation and regeneration of damaged tissue cells [15,16]. Adding to this, each TPMS structure has no self-intersecting or enfolded surfaces which enable them to be patterned into a 3-dimensional space [17]. Previous literature has investigated the use of nine different TPMS architecture for tissue scaffold design [18]. The Schwarz P (Primitive) TPMS structure makes one of them [19,20]. The Schwarz P structure is characterized to exhibit a high load bearing capacity due to its inherent strain distributions [21]. Investigations characterizing the mechanical properties of a Schwarz P structure through compressive loading has determined optimal stress distributions compared to other TPMS structures [22]. In addition, the Schwarz P structure has also been characterized to have the largest fluid permeability compared to other TPMS structures [23]. In due regards to this, tissue scaffolds implementing the Schwarz P architecture has the potential to fulfill biological design criteria in terms of transport properties. With inherent circular cross-sectional surfaces, the Schwarz P architecture makes an ideal pore morphology for scaffold fabrication [16].

This study investigates the computational mechanical characterization of Schwarz P unit cell-based tissue scaffolds fabricated via two-photon polymerization (2PP) in the context of geometrical transformations. These tissue scaffolds have been fabricated from methacrylated poly(D,L-lactide-co- ε -caprolactone) (PLCL) copolymer with a lactide (L) to caprolactone (C) molar ratio of 16:4 i.e. LCM3, via two-photon polymerisation (2PP) as part of the European Union Research and Innovation 7th Framework Program under grant agreement no. 2633 63 (INNOVABONE) with TETRA-Society for Sensoric, Robotics and Automation GmbH (Ilmenau, Germany) using an input stereolithography file of a Schwarz P unit cell model. Previous investigations performed under the INNOVABONE project has found geometrical transformations between the intended original Schwarz P unit cell design and the unit cells comprising the physical fabricated tissue scaffolds. This study seeks to justify the implementation of micromechanical analysis as a reliable approach to computationally characterize the mechanical properties of Schwarz P unit cell-based tissue scaffolds despite the geometrical transformations that have occurred. Validating the data against experimental results and subsequently justifying the approach would emphasize the flexibility of micromechanical analysis in accommodating potential occurrences of geometrical transformation as a result of fabrication via additive manufacturing. In cases where the geometrical transformations can be predicted, micromechanical analysis can be simply employed to characterize resulting mechanical properties of a tissue scaffold with a periodic microstructure. This would effectively shorten mechanical testing stages to make time for biological characterization if the mechanical properties were found to be desirable.

Only a few studies have been performed in regards to computational mechanical characterization of tissue scaffolds based on the Schwarz P TPMS architecture. Two such studies, performed by Shin et al (2012) considered a phase-field model; and a more recent study by Huang et al which considered a multiscale modeling approach [22,24]. This study investigates Schwarz P unit cell-based tissue scaffolds in the context of their fabrication via 2PP and computational mechanical characterization via micromechanical analysis.

2. Materials and methods

2.1. Scaffold design and fabrication

A Schwarz P unit cell packaged into a stereolithography (.STL) file was used as an input to fabricate its formation into a lattice to form tissue scaffolds via two-photon polymerization (2PP). Limitations of the file format for use in computational models required the. STL file to be 'reverse engineered' into a useable surface geometry CAD model. Through Altair Hyperworks 14.0 (Altair Engineering Inc., Michigan, USA), surfaces were manually created by utilizing vertices between different triangles comprising the triangulations of the. STL model. A comparison of the. STL file and the surface geometry CAD model is shown in Fig. 1.

2PP involves the initiation of femtosecond laser pulses on photosensitive or photoresistive materials resulting in two-photon absorption and subsequent material polymerization. Schwarz P unit cell-based lattice tissue scaffolds have been fabricated using materials based on methacrylated poly(D,L-lactide-co- ε -caprolactone) (PLCL) copolymer with a lactide (L) to caprolactone (C) molar ratio of 16:4 i.e. LCM3.

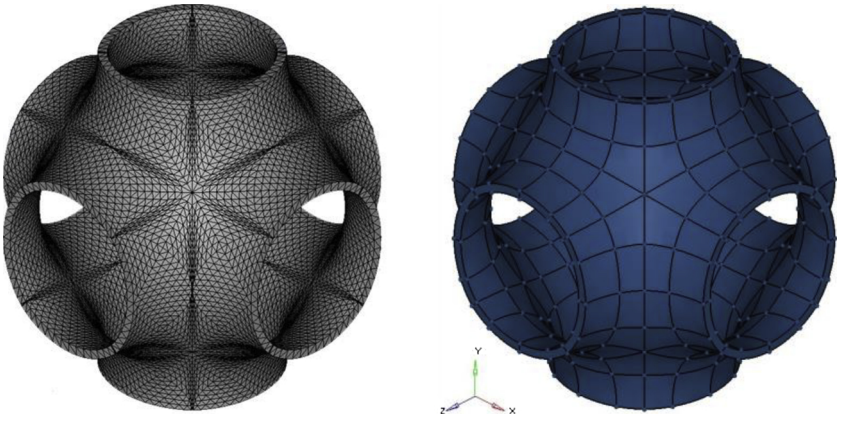

Fig. 1. Surface geometry CAD model (right) of a Schwarz P unit cell after 'reverse engineering' its stereolithography model (left).

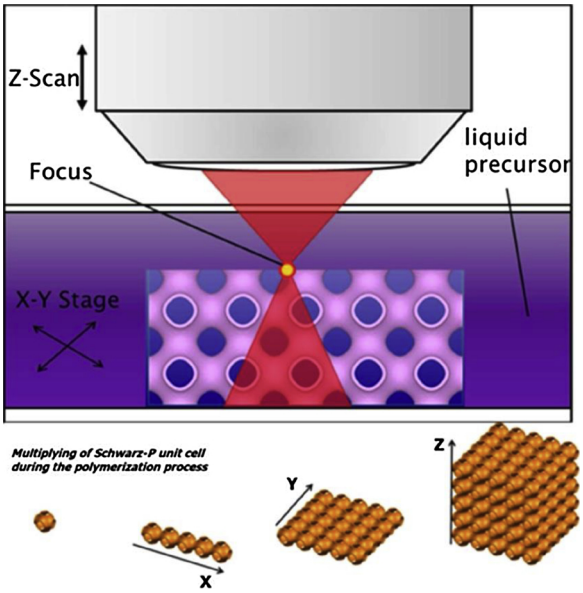

Fig. 2. Schematic presentation of the two-photon polymerization (2PP) fabrication process of Schwarz P unit cell lattice tissue scaffolds. A positioning stage moves in the x and y direction while the focus beam translates in the z direction. Polymerization of the liquid precursor occurs in accordance to the computer model i.e. STL model of the Schwarz P unit cell with the support of a galvano-scanner. The result of the 2PP fabrication process in a 4 × 9 × 4 unit cell array in the x, y and z direction respectively [21].

Syntheses of the liquid precursor making up the photoresist for scaffold material considered have been detailed in previous literature [21].

A femtosecond laser source with 800 nm wavelength pulsating at 140 fs at 80 MHz repetition rate (VISION II, Coherent, Scotland) was used as part of the 2PP apparatus (M3DL, LZH Hannover, Germany). The focus of the laser beam was equipped with an x63 objective lens and a numerical aperture (NA) of 0.75 (LD-Plan-NEOFLUAR, Zeiss, Germany). During laser pulses into the photoresist, a tri-axial positioning stage dynamically moves in tolerance of nanometers according to the .STL model of the Schwarz P unit cell with the support of a galvano-scanner (Aerotech, USA). The result is an array of 4 × 9 × 4 unit cells in the x, y and z directions respectively [21]. A graphical schematic of the 2PP process is shown in Fig. 2. An SEM micrograph of the fabricated tissue scaffold is shown in Fig. 3.

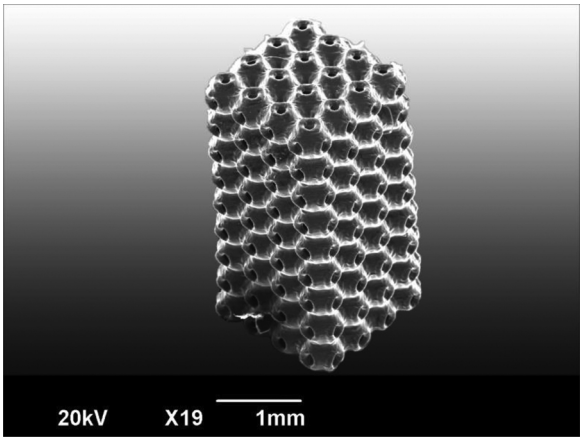

Fig. 3. SEM micrograph of a fabricated physical Schwarz P unit cell-based tissue scaffold.

2.2. Scaffold experimental mechanical characterization

Mechanical characterization of fabricated Schwarz P unit cell-based lattice tissue scaffolds involved compression experiments performed using a Hounsfield testing machine. Scaffold samples were compressed to 20% strain from its original height at a crosshead speed of 0.5 mm min^{-1} with a 5 N load cell. The compression was restricted to 20% strain to prevent permanent deformation of the scaffolds and allow for full recovery. The stiffness i.e. compressive modulus, representative of the mechanical property was determined based on the equation of a linear region formed at low strain values of the stress-strain curve obtained from the compression experiment.

2.3. Scanning Electron microscope (SEM) microscopy

2.3.1. Scanning procedure

Scaffold samples that had not undergone compression were coated with platinum using a Polaron SC7640 coater (Quorum Technologies, UK) at 2.2 kV for 90 s A JEOL JSM-6490LV SEM microscope was then used to image the top and side surfaces of the samples. Each view perspective i.e. the top and two sides of the scaffold were assigned a specific directional plane axis. This allows the nomination of a dimensional parameter which will be referenced for a particular measurement for each directional axis on a particular plane axes i.e. horizontal and vertical. Due to the nanoscale size and soft nature of the samples, it was not possible to make cross-sectional cuts without any accidental perturbations to the original structure. Therefore, measurements were restricted to observable unit cells on the external sides of the sample.

2.3.2. Measurement analysis

SEM micrographs obtained were implemented for use in an averaging technique to obtain a micrograph containing an average of all observable unit cells with respect to different view perspectives i.e. plane axes. Considering a SEM micrograph taken at a respective plane axes, each observable unit cell were ‘cut’ through ImageJ (National Institute of Health, USA) and saved as a separate graphic file without any changes in resolution. A collection of unit cell micrographs was thus obtained respective of the plane view considered. A custom Python algorithm was used to transpose the center point of each unit cell micrograph (defined by the center point of the internal pore diameter) on a blank canvas to standardize the different image dimensions. A separate custom Python algorithm was then used to average the unit cell micrographs with black backgrounds and an averaged unit cell SEM micrograph was subsequently obtained. Dimensional parameters which include the height, width, length and wall thickness were measured using available tools in ImageJ based on the nominations made during the scanning procedure. A complete guideline in performing the SEM-based averaging has been appended in Supplementary Material S.1.

2.4. Schwarz P unit cell CAD model reconstruction

CAD modeling techniques were applied to reconstruct the Schwarz P unit cell model based on measurements of dimensional parameters obtained from the averaged unit cell SEM micrograph. This gives a unit cell which approximately represents an average of observable unit cells comprising the fabricated tissue scaffold while also taking into account geometrical transformations. Implementing a computational approach for mechanical characterization on the reconstructed unit cell model should thus give a more accurate representation of unit cells comprising the fabricated tissue scaffolds and subsequently allow a more faithful comparison to experimental mechanical characterization. Reconstruction was generally performed on the Schwarz P unit cell surface geometry CAD model through available tools in Altair Hyperworks (Altair Engineering Inc., Michigan, USA).

2.5. Micromechanical analysis

Micromechanical analysis has its foundation in idealizing a structure consisting of a periodic microstructure as a crystal packing system. Geometrical symmetries can be subsequently exploited to determine a representative unit cell i.e. Voronoi cell. This would thus reduce mechanical characterization of a tissue scaffold with a periodic unit cell microstructure to the analysis of a single representative unit cell through derivations of boundary conditions. Macroscopic loads in terms of stresses or strains can be applied along with the boundary conditions before evaluation of the effective properties of the structure in question.

2.5.1. Selection for crystal packing system & representative unit cell

Several typical packing systems have been examined in previous literature [25]. The fabrication of scaffolds considered in this study involved a simple 3-dimensional translation of the Schwarz P unit cell model. Based on the aforementioned literature in regards to the above and taking into account the uniform height, width and length inherent in the Schwarz P architecture, the tissue scaffold can be idealized as a 'simple cubic packing' system with the Schwarz P unit cell themselves the representative 'cubic' unit cell. However, in the context of geometrical transformations, unit cells comprising the fabricated tissue scaffold consists of non-uniform height, width and length. Therefore, a cuboidal variation of the 'simple cubic packing' system i.e. 'simple cuboidal packing' system with the reconstructed unit cell model as the representative 'cuboidal' unit cell is more appropriate for idealization.

2.5.2. Derivations for boundary conditions

The reconstructed unit cell represented as a 'cuboid' in a 'simple cuboidal packing' system is shown in Fig. 4.

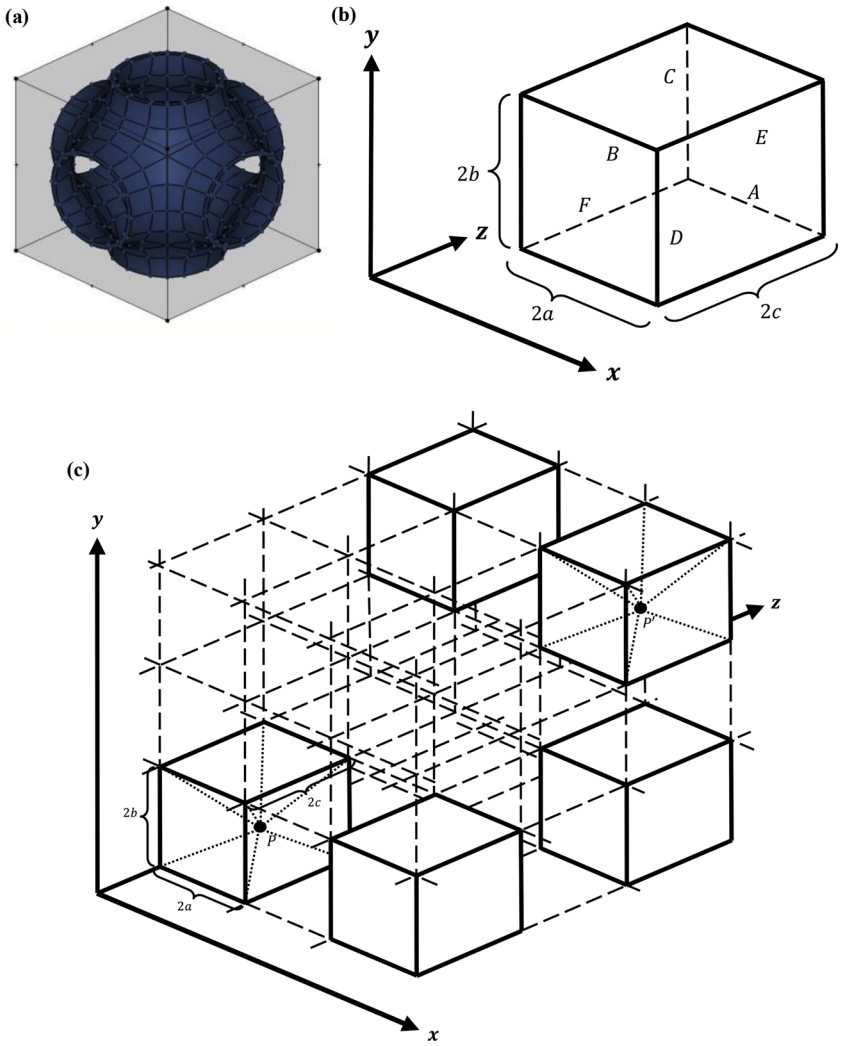

Fig. 4. (a) Example of a unit cell with non-uniform height, width and length i.e. cuboidal dimensions fitting into a cuboid as a representative unit cell; (b) Simple cuboid representing the reconstructed unit cell model taking height, width and length measurements obtained from measurement analyes made from the averaged unit cell SEM micrograph (respective of the plane axes). Translating the cuboid i.e. reconstructed unit cell into a 3-dimensional array gives a more realistic representation of fabricated tissue scaffold as shown in Fig. 3; (c) Simple cuboidal packing system consisting of an array of cuboids/reconstructed unit cells translated in a 3-dimensional direction.

Through translational symmetries, the application of macroscopic stresses or strains on a single unit cell is applied identically to other unit cells as representative images of the unit cell being considered. With this, the macroscopic strains and the relative displacements at a particular point in a unit cell is mathematically related to the image of that point in another unit cell in accordance to Eq. (1).

$$\begin{aligned} u' - u &= (x' - x)\varepsilon_x^0 + (y' - y)\gamma_{xy}^0 + (z' - z)\gamma_{xz}^0 \\ v' - v &= (y' - y)\varepsilon_y^0 + (z' - z)\gamma_{yz}^0 \\ w' - w &= (z' - z)\varepsilon_z^0 \end{aligned} \tag{1}$$

for which,

x, y and z :	Coordinates of point P
u, v and w :	Displacements associated with point P
x', y' and z' :	Coordinates of the point P'
u', v' and w' :	Displacements associated with point P'
ε_x^0 , ε_y^0 , ε_z^0:	Macroscopic strains
γ_{yz}^0 , γ_{xz}^0 , γ_{xy}^0 :	Macroscopic shear strains

Constraining the displacements where $u = v = w = 0$ at any arbitrary point in a unit cell eliminates rigid body translations in a 3-dimensional direction and thus allow Eq. (1) to be obtained. Rotations of the x-axis about the y-axis and the z-axis and the rotations of the y-axis about the x-axis are constrained such that $\partial w/\partial x = \partial v/\partial x = \partial w/\partial y = 0$ at $x = y = z = 0$. With the above, Eq. (1) can then be implemented further to derive the necessary displacement boundary conditions in conjunction to a selected packing system.

Consider point P in a representative 'cuboidal' unit cell and its image, P' in another representative unit cell translated in a 3-dimensional direction as presented in Fig. 4(c). Point P' can be determined by translational symmetry transformations as shown in Eq. (2).

$$(x',\ y',\ z') = (x + 2ia,\ y + 2jb,\ z + 2kc) \tag{2}$$

for which i, j and k are the number of representative cuboidal unit cells in which P' is translated from P in the x, y and z directions respectively. The faces of a representative cuboidal unit cell can thus be paired by transformations tabulated in Table 1. Substituting the equations established in Table 1 into Equation (1), the displacement boundary conditions for each of faces is tabulated in Table 2.

Table 1
Equations defining the pairing between opposite faces of a representative cuboidal unit cell. For cubic unit cells in a simple cubic packing system, the values of a, b and c are equivalent i.e. a = b = c.

Faces A and B	$x = a$ for face A	$x = -a$ for face B	$i = 1; j = k = 0$
Faces C and D	$y = b$ for face C	$y = -b$ for face D	$j = 1; i = k = 0$
Faces E and F	$z = c$ for face E	$z = -c$ for face F	$k = 1; i = j = 0$

The displacement boundary conditions tabulated in Table 2 are applied to nodes of the faces of the discretized reconstructed unit cell model wherein the notations $|_{y,z}$, $|_{x,z}$ and $|_{x,y}$ indicate common directional axes of tessellated faces between each pair. Since no two faces share a common edge in a Schwarz P unit cell and the reconstructed unit cell mode, no further boundary conditions need to be established in regards to this. Therefore, only the displacement boundary conditions for the faces are required for implementation of micromechanical analysis. Implementation of the displacement boundary conditions along with applied macroscopic stress would give results in terms of average strains and average shear strains. Based on the results, the effective properties can subsequently be determined in accordance to previous literature [25].

Table 2
Displacement boundary conditions for simple cuboidal packing system. Similar to a simple cubic packing system with a cubic representative unit cell, 3 different pairs of faces are obtained from 6 different faces. In the case of a simple cubic packing system, the variables a, b and c are equivalent.

Pair faces	Displacement boundary conditions
A and B	$\lvert u_A - u_B\rvert_{y,z} = 2a\varepsilon_x^0$ $\lvert v_A - v_B\rvert_{y,z} = 0$ $\lvert w_A - w_B\rvert_{y,z} = 0$
C and D	$\lvert u_C - u_D\rvert_{x,z} = 2b\gamma_{xy}^0$ $\lvert v_C - v_D\rvert_{x,z} = 2b\varepsilon_y^0$ $\lvert w_C - w_D\rvert_{x,z} = 0$
E and F	$\lvert u_C - u_D\rvert_{x,z} = 2c\gamma_{xz}^0$ $\lvert v_C - v_D\rvert_{x,z} = 2c\gamma_{yz}^0$ $\lvert w_C - w_D\rvert_{x,z} = 2c\varepsilon_z^0$

2.5.3. Validation method for correct implementation of displacement boundary conditions

Correct implementation can be assessed through the results for average strain and average shear strain results. Tabulating the results for average strain values should give symmetric results along the diagonal with differing values in the diagonal. The same also applies for tabulated results of average shear strain with the exception that the values lying outside the diagonal can be approximated to zero due to their small values. Tabulated representation of the above is appended in Appendix A (Tables A1 and Table A2).

2.5.4. Reconstructed unit cell model discretization and material model assignment

The reconstructed unit cell model was discretized into second-order tetrahedral, C3D10 elements. With displacement boundary conditions being established between pairs of faces, discretization of a pair of faces lying along a common directional axes must be identical. This was obtained through tools available in Altair Hyperworks. The reconstructed unit cell model was assumed to take homogenous, isotropic and linearly elastic material properties of LCM3. The lower limit (4.39 MPa), averaged (5.74 MPa) and the upper limit (6.65 MPa) modulus values of LCM3 was obtained from compression experiments of bulk LCM3 cylinders while the Poisson's ratio was taken to be 0.3. The bulk material data has been appended as Supplementary material in Supplementary Material S.2.

3. Results

3.1. Experimental characterisation of tissue scaffold

Graphical presentation of stress-strain data for all five specimens obtained from compression experiments are presented in Fig. 5.

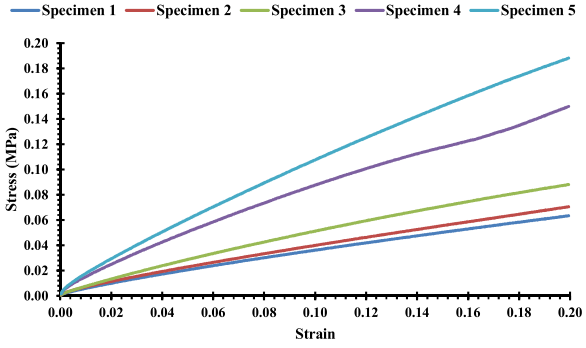

Fig. 5. Stress-strain curves for all 5 specimens of fabricated Schwarz P unit cell-based tissue scaffolds obtained from compression experiments. Compression was only performed at a maximum 20% strain from its original height to prevent permanent deformation of scaffolds.

Based on consideration of the linear region (lying immediately after the 'toe region'), the stiffness i.e. modulus of fabricated Schwarz P unit cell-based tissue scaffolds were averaged at 0.69 ± 0.29 MPa with an obtainable maximum of 1.14 MPa and a minimum of 0.40 MPa.

3.2. SEM measurement analysis & reconstructed unit cell model

With the SEM measurement analysis performed, it can be confirmed that geometrical transformations have occurred between the input Schwarz P unit cell design and the unit cells comprising the fabricated tissue scaffold. More specifically, the geometrical transformations that have occurred are in the form of shrinkage. Measurements also showed non-uniformity between height, width and length along with increased wall thickness compared to the original design. A comparison of measurements for the parameters mentioned between the original Schwarz P unit cell design and the unit cell averaged from the fabricated tissue scaffold is shown in Tables 3 and 4.

Table 3
Comparison of height, width and length measurements of the averaged unit cell SEM micrograph (averaged from unit cell micrographs comprising the fabricated tissue scaffold) and the intended Schwarz P unit cell design. Averaging of the SEM micrographs produces a single micrograph with respect to the plane view in consideration. However, one dimensional parameter can be represented in two different plane view i.e. two micrographs. Calculating the mean average for that particular dimensional parameter would also give the standard deviation.

Parameter	Measurement (Mean ± Standard deviation) (mm)	
	Average of unit cells comprising fabricated scaffolds	Intended Schwarz P unit cell design
Height	0.389 ± 0.008	0.520
Width	0.403 ± 0.018	0.520
Length	0.413 ± 0.008	0.520

Table 4
Comparison of wall thickness measurements between the averaged unit cells comprising the fabricated tissue scaffold (obtained from measurements analysis of the averaged SEM micrograph) and the intended Schwarz P unit cell design.

Plane	Wall Thickness Measurement (Mean ± Standard deviation) (mm)	
	Average of unit cells comprising fabricated scaffolds	Intended Schwarz P unit cell design
YX	0.0280 ± 0.018	0.0139
YZ	0.0288 ± 0.016	0.0139
XZ	0.0450 ± 0.000	0.0139

To take into account the geometrical transformations, the mean values for height, length and wall thickness measurements were used to reconstruct the Schwarz P unit cell surface geometry CAD model through the software Altair Hyperworks. This gives a unit cell that approximately represents the average of unit cells comprising the fabricated tissue scaffold. It shall be noted here that the reconstruction was performed with the assumption that the average unit cell is of quarter symmetry to allow the implementation of micromechanical analysis. The surface geometry CAD model of the reconstructed unit cell model is shown in Fig. 6.

3.3. Micromechanical analysis

Application of micromechanical analysis in the context of a linear material model assigned to the reconstructed unit cell (model A) gave results in terms of average strain and average shear strains. The results for average strains and average shear strains comply with the validation methods for correct implementation of displacement boundary conditions. Tabulated results for this in regards to the compliance for validation can be referred to in Appendix B (Tables B1 and Table B2). The effective modulus was determined based on the average strain results obtained and is graphically presented in Fig. 7 along with the experimental modulus range obtained. The effective modulus of the original Schwarz P unit cell (model O) is also presented. Since physical tissue scaffolds were compressed height-wise (along the y-axis) before determining the experimental stress-strain curve and subsequent modulus,

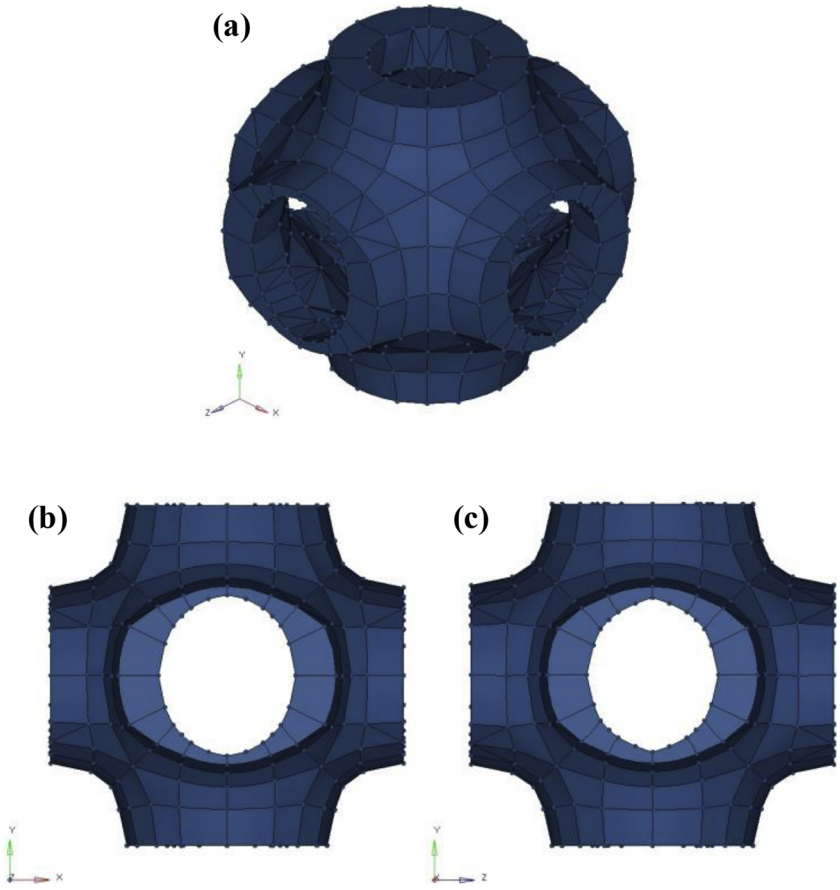

Fig. 6. Graphical presentation of the reconstructed unit cell model. The Schwarz P unit cell model was reconstructed based on mean measurements previously established with the discussed CAD modeling techniques. (a) General view of the reconstructed unit cell; (b) YZ plane view of the reconstructed unit cell; (c) YZ plane view of the reconstructed unit cell.

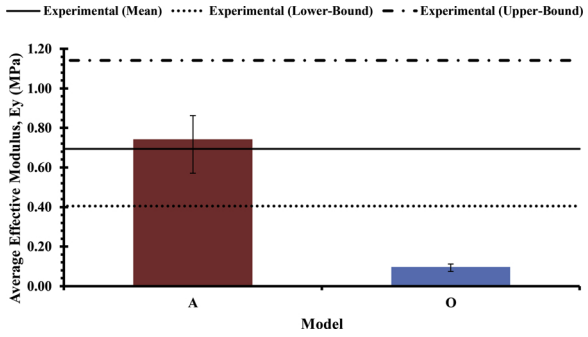

Fig. 7. Average effective modulus determined from average strain results (in the 2nd degree of freedom) between the reconstructed unit cell (model A) and the experimental modulus values obtained in Sub-section 4.1. The average effective modulus of the original Schwarz P unit cell (model O) is also presented in the chart. The error bars represent the respective lower and upper limit effective modulus values obtained. The experimental modulus results are represented as horizontal lines according to the lower limit, average and upper limit values obtained from compression experiments of fabricated tissue scaffolds.

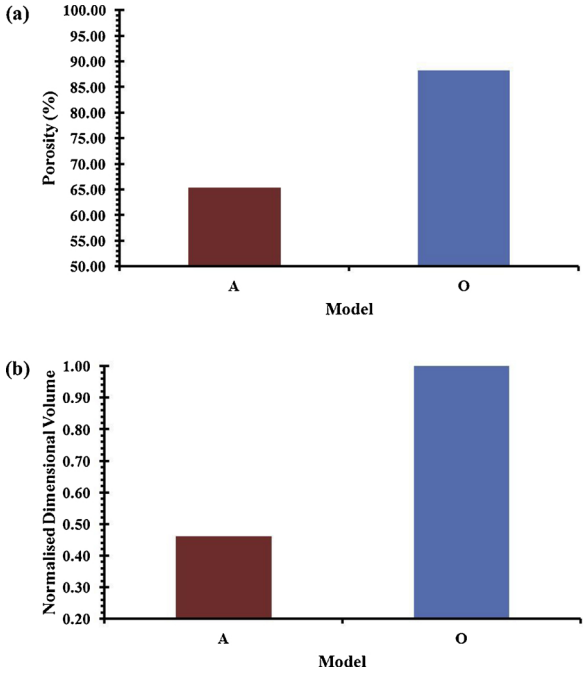

Fig. 8. Graphical comparison between (a) porosity and; (b) normalized dimensional volume between the reconstructed unit cell model (model A) and the original Schwarz P unit cell (model O).

it shall be noted here that only the effective modulus with respect to the y-axis is considered.

The effective modulus of the reconstructed unit cell model (model A) falls within the experimental range of modulus values for which model A over-estimates the mean experimental modulus value by 6.94%. On the other hand, the original Schwarz P unit cell (model O) on the other hand differs by 86.05% from the experimental mean. To further understand the relationships between different dimensional parameters and the resulting effective modulus, several parameters were derived to allow comparison between model A (which represents unit cells comprising the fabricated tissue scaffolds after subsequent geometrical transformations) and the original Schwarz P unit cell design, model O. The dimensional volume (simple product of height, width and length) is normalized to that of model O. The same applies for the wall thickness and radius of curvature with respect to different

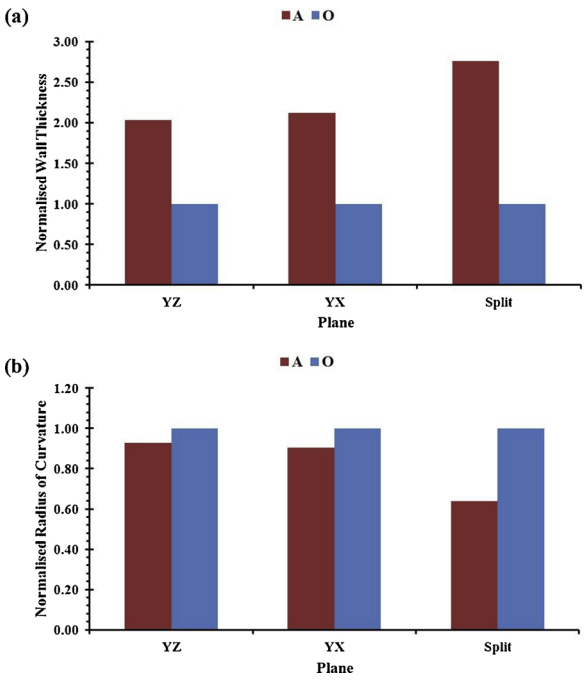

Fig. 9. Graphical comparison of the (a) normalized wall thickness and; (b) normalized radius of curvature between the reconstructed unit cell (model A) and the original Schwarz P unit cell (model O). The wall thickness and radius of curvature measurements with respect to different cross-sectional planes for the reconstructed unit cell model are normalized against the original Schwarz P unit cell model. Hence, the normalized wall thickness and normalized radius of curvature for model O is equivalent to 1.

cross-sectional planes (graphically presented in Fig. C1 of Appendix C) from which measurements are made. The methodology for measurements of the wall thickness and radius of curvature are also detailed in Appendix C. Comparison of different derived parameters between model A and O are presented in Fig. 8 and Fig. 9.

Considering Fig. 8(a), the porosity of the original Schwarz P unit cell model is compared to the reconstructed unit cell model. The same also applies in terms of the dimensional volume as implied from the normalized dimensional volume in Fig. 8(b). Comparisons show that the porosity and normalized dimensional volume of the reconstructed unit cell is smaller compared to the original Schwarz P unit cell model. Model A having a smaller normalized dimensional volume compared to model O implies that the reconstructed unit cell has a smaller overall size compared to the original Schwarz P unit cell while the low porosity of model A suggests lesser amount of pore space within the confined of the unit cell construct. The normalized wall thickness measured at different cross-sectional planes of the reconstructed unit cell model is consistently thicker compared to the original unit cell model as shown in Fig. 9(a). However, the opposite is observed in consideration of the normalized radius of curvature. The normalized wall thickness measured at different cross-sectional planes was determined to be consistently lower compared to the original unit cell model as shown in Fig. 9(b). The dimensional parameters considered would theoretically influence the resulting stiffness of the unit cell and subsequently its array into a tissue scaffold construct. In addition, these parameters can also compensate with one another to influence the resulting effective modulus. This will be discussed further in the discussions.

4. Discussion

4.1. Geometrical transformations

Initial investigations performed under the INNOVABONE project has found geometrical transformations between the intended Schwarz P

Table 5
Evaluation of ratios between cube of normalized radius of curvature and the normalized wall thickness along plane YZ and YX; and the normalized radius of curvature along the split plane for the reconstructed unit cell and the original Schwarz P unit cell model. Rank numberings (showed in brackets) indicate the expectancy for higher values of deflections i.e. low modulus values.

Model	Ratio between cube of normalised radius of curvature and the normalised wall thickness		Normalised radius of curvature
	Plane YZ	Plane YX	Split plane
O	1 (1)	1 (1)	1 (1)
A	0.3940 (2)	0.3493 (2)	0.638 (2)

unit cell design and the unit cells comprising the 2PP-fabricated tissue scaffold structure [21]. Measurement analyses made on averaged unit cell SEM micrograph of the scaffolds in this study complements the aforementioned investigation. Emphasizing further, it was determined based on the measurements that the geometrical transformations show the occurrence of shrinkage. The 2PP fabrication process parameters can generally be considered as the main source of discrepancy i.e. geometrical transformations and shrinkage.

Polymerization is known to be accompanied by a reduction in the total volume of material in a phenomenon known as volumetric or polymerization shrinkage [26]. Despite shrinkage being an important role in the fabrication of tiny structure with high resolution features, it does become an obstacle in the fabrication of complex structures [9]. In the context of implementing scaffolds with seeded cells, tissue scaffolds comprising of porous structures undergoing shrinkage would consequently lead to smaller pores for the movement of cells throughout the confines of scaffolds. This would lead to insufficient cell growth and cellular activity when cells are seeded within the tissue scaffold construct. 2PP works in a lay-by-lay method which involves the stacking of the fundamental element – voxels [4]. A voxel (also known as a volumetric pixel) is defined as the unit volume of a material cured by 2PP [7]. Hence, the accuracy of a structure fabricated via 2PP is thus dependent on the voxels and their respective feature size [9]. During fabrication, the activation energy i.e. polymerized threshold fluence exceeds the threshold dose of a photoresist after a threshold exposure time to form polymerized voxels around the light intensity maximum of the focal spot [6,27]. These polymerized voxels expand in an anisotropic direction where the expansion is greater along the axial direction compared to that along the focal plane [6]. Shrinkage also occurs due to the solid phase having a higher mass density during the liquid phase during polymerization [4]. With the above, the effects between the anisotropic voxel growth and the differences in mass density can be implied to occur in tandem of one another and/or in isolation. Despite the overall shrinkage found from measurement analyses of the averaged unit cell, the measurements also showed that the height is smaller compared to the width and length. This would potentially imply the compounding effect mentioned previously.

Shrinkage has been reported to be a side effect of working in the sub-diffraction regime when the polymerized volume is minimized from the reduction in monomer-to-polymer conversation rate suggesting the influence of the degree of polymerization on the shrinkage rate [9]. The degree of polymerization rate on the other hand is subsequently influenced by both laser power and writing speed. Studies investigating the dependency of laser power on the degree of polymerization have shown that the laser power is indicative of the amount of energy supplied for polymerization i.e. polymerized threshold fluence which affects the resulting overall shrinkage of a fabricated structure. One previous study investigating the shrinkage of Zr-based hybrid photosensitive materials produced by 2PP found that at laser powers below a certain threshold resulted in shrinkage of the overall dimensions of fabricated structures [28]. This complemented another study which concluded that the ultimate shrinkage and shrinkage rate are both dependent on the amount of energy required for polymerization [29].

The influence of writing speed is implied through the time between pulses of femtosecond laser i.e. exposure time in which increased writing speeds would corresponds to lower exposure times [30]. The growth of polymerized voxels in terms of diameter and height has been mathematically expressed to be a function of power and time; and experimentally characterized through line writing experiments [30–33]. Line writing experiments evaluating the expansion of voxels in terms of width with respect to writing speed has generally shown that higher writing speeds resulted in thinner polymerized line widths. This complements investigations performed under the INNOVABONE project [34]. Therefore, the writing speed potentially has some contribution to the shrinkage. It is possible that writing speeds higher than ideal subsequently resulted in thin polymerized line widths and eventually smaller than intended gross build-up of voxels making up the fabricated structure.

4.2. Influence of dimensional parameters

The wall thicknesses and radius of curvature defining the predominant surface curvature inherent in the Schwarz P architecture provides bending resistance for the structure under compression and subsequently affects the resulting effective modulus. Bending resistance for surface curvatures connecting two adjacent pores can be described in term of Castigliano's theorem for curved thin beams [35]. Here, the resulting deflection is dependent on the ratio between the cube of the radius of curvature, R^3 and the moment of inertia, I (particularly related to the wall thickness). Hence compensation for effective modulus can be implied to occur between these two parameters. A high R at constant I gives higher amount of deflections and subsequently lower bending resistance i.e. lower effective modulus. Thicker walls give higher values of I which compensate to give lower deflections and therefore increasing bending resistance i.e. higher effective modulus. Bending resistance for surface curvatures connecting two opposite pores can be described in terms of Euler buckling theorem for initially curved beams [35,36]. Here, the radius of curvature, R is a scaling factor contributing to the resulting maximum lateral deflection for which higher values of R gives higher deflections. Higher values of deflections give way to lower bending resistance and subsequently lower effective modulus values.

A ranking system was established in regards to the above to show the expectations of how one model succeeds another in terms of the effective modulus in conjunction to the parameters considered. The reconstructed unit cell and the original Schwarz P unit cell model was ranked between 1 and 2, with the ranking numbers indicating the expectancy for lower values of deflections i.e. high modulus values. Hence, a ranking of 2 implies low deflections and a resulting higher modulus values. The rankings are tabulated in Table 5.

Based on the rankings in Table 5, it can be observed that the normalized wall thickness and/or normalized radius of curvature of the original Schwarz P unit cell model consistently succeeds the reconstructed unit cell model for high deflections at different cross-sectional planes. It can be deduced here the original Schwarz P unit cell is expected to have a lower effective modulus than the reconstructed unit cell.

Further adding to the above, the porosity and dimensional volume also affects the resulting effective modulus. At constant porosity between different unit cell models, a smaller dimensional would imply smaller amount of void space within the confines of the unit cell and subsequently overall tissue scaffold construct available for compression. With constant application of load across the different models consisting of the same material, the unit cell with the smaller dimensional volume would give higher modulus values. The original Schwarz P unit cell design has a larger dimensional volume and a porosity value that is 25.96% higher compared to that of the reconstructed unit cell. Hence, it can be deduced that the original Schwarz P unit cell is expected to have

a lower effective modulus than the reconstructed unit cell. This adds into effect with the theoretical expectation that the original design should have a lower effective modulus due to its attribution in terms of the wall thickness and radius curvature in regards to the inherent surface curvatures. Results obtained from micromechanical analysis of the reconstructed unit cell and original Schwarz P unit cell confirm the theoretical expectations discussed above. Since the unit cell was reconstructed to approximately represent the average of all unit cells comprising the fabricated tissue scaffold, the experimental model also indirectly confirms the theoretical expectations.

5. Conclusion

Geometrical transformations as a result of non-uniform shrinkage have been taken into account by reconstructing the Schwarz P unit cell surface geometry model to approximately represent the average of unit cells comprising the fabricated tissue scaffolds. Micromechanical analysis of the reconstructed unit cell assigned with the same material model making up the fabricated Schwarz P unit cell-based tissue demonstrated excellent agreement to experimental mechanical characterization in terms of modulus with only a small margin error of 6.94%; a stark comparison to the original intended design which gave an error of 86.05% from the experimental mean modulus. Emphasizing this, micromechanical analysis was able to be implemented despite the geometrical transformations by simply taking them into account in derivations for boundary conditions and in terms of CAD modeling.

The above would thus validate the use of micromechanical analysis in the context of the tissue scaffold considered in this study. With various different crystal packing systems which can be used to idealize structures with periodic microstructures, micromechanical analysis can be applied to other regular tissue scaffold structures. Furthermore, the approach can also be applied to computationally characterize the mechanical properties of structures outside the field of bone tissue engineering depending on their idealization to crystal packing systems. Considering that the micromechanical analysis has a foundation in reducing a structure to a periodic microstructure to the analysis of a single representative unit cell based on derivations of boundary conditions, efficiency in terms of time and computational resources is maintained.

Acknowledgements

The authors would like to thank our colleagues at the TETRA Society for Sensoric, Robotics and Automation GmbH (Germany) and the Institute for Bioprocessing and Analytical Measurement Techniques (Germany) for providing all the samples involved in this study. This research project is funded by the European Union's 7th Framework Program under grant agreement no. 2633 63 (INNOVABONE). This work was supported by the Engineering and Physical Sciences Research Council [grant number EP/K029592/1]; and the EPSRC Centre for Innovative Manufacturing in Medical Devices (MeDe Innovation).

Appendix A

The average strains and average shear strain results are used to validate correct implementation of the displacement boundary conditions for micromechanical analysis. For boundary conditions derived for a simple cuboidal packing system, the tabulated average strains and average shear strains results should be as shown in Table A1 and Table A2 respectively. The average strains are symmetric along the diagonal with differing values within the diagonal. The same applies for average shear strains however, the values lying outside the diagonal can be approximated to zero due to their small values.

Table A1
Tabulated representation of average strain values from micromechanical analyses to validate displacement boundary conditions established for a simple cuboidal packing system.

Degree of freedom of load/displacement application	Average strain		
	x	y	z
ε_x^0	ε_1	ε_2	ε_3
ε_y^0	$\varepsilon_4 (\approx \varepsilon_2)$	ε_5	ε_6
ε_z^0	$\varepsilon_7 (\approx \varepsilon_3)$	$\varepsilon_8 (\approx \varepsilon_6)$	ε_9

Table A2
Tabulated representation of average shear strain values from micromechanical analyses to validate displacement boundary conditions established for a simple cuboidal packing system.

Degree of freedom of load/displacement application	Average shear strain		
	x	y	z
γ_{yz}^0	γ_1	0	0
γ_{xz}^0	0	γ_2	0
γ_{xy}^0	0	0	γ_3

Appendix B

Micromechanical analysis of the reconstructed unit cell model gave average strains and average shear strains that complied with the validation methods for correct implementation of displacement boundary conditions. The average strains and average shear strains are tabulated in Table B1 and Table B2 respectively.

Table B1
Average strain values obtained from micromechanical analysis of discretised reconstructed unit cell model assigned with 3 different LCM3 material models i.e. lower limit (specimen 5), the average and upper limit (specimen 3). The unit cell was reconstructed to approximately represent an average of unit cells comprising the fabricated tissue scaffold. The average strains for each material model are symmetric along the diagonal with differing values within the diagonal. This thus complies with the validation methods for correct implementation of displacement boundary conditions derived for the simple cuboidal packing system in revised micromechanical analysis.

Material model	Degree of freedom of load application	Average strain		
		x	y	z
Specimen 5 (Lower limit)	ε_x^0	0.102	0.0591	0.0123
	ε_y^0	0.0591	0.135	0.0527
	ε_z^0	0.0123	0.0527	0.0897
Average	ε_x^0	0.0787	0.0454	0.00945
	ε_y^0	0.0454	0.104	0.0405
	ε_z^0	0.00945	0.0405	0.0689
Specimen 3 (Upper limit)	ε_x^0	0.0677	0.0391	0.00813
	ε_y^0	0.0391	0.0894	0.0348
	ε_z^0	0.00813	0.0348	0.0593

Table B2
Average shear strain values obtained from micromechanical analysis of discretised reconstructed unit cell model assigned with 3 different LCM3 models i.e. specimen 5 (for the lower limit), the calculated average and specimen 3 (for an upper limit). The average shear strains for each material model are symmetric along the diagonal with differing values within the diagonal. Values outside the diagonal can be approximated to zero. This thus complies with the validation methods for correct implementation of displacement boundary conditions derived for the simple cuboidal packing system in revised micromechanical analysis.

Material model	Degree of freedom of load application	Average shear strain		
		x	y	z
Specimen 5 (Lower limit)	γ_{yz}^0	0.122	4.754E-8 (≈0)	2.088E-7 (≈0)
	γ_{xz}^0	4.754E-8 (≈0)	0.176	3.782E-7 (≈0)
	γ_{xy}^0	2.088E-7 (≈0)	3.782E-7 (≈0)	0.125
Average	γ_{yz}^0	0.0939	3.653E-8 (≈0)	1.605E-7 (≈0)
	γ_{xz}^0	3.653E-8 (≈0)	0.135	2.906E-7 (≈0)
	γ_{xy}^0	1.605E-7 (≈0)	2.906E-7 (≈0)	0.0957
Specimen 3 (Upper limit)	γ_{yz}^0	0.0807	3.141E-8 (≈0)	1.380E-7 (≈0)
	γ_{xz}^0	3.141E-8 (≈0)	0.116	2.499E-7 (≈0)
	γ_{xy}^0	1.380E-7 (≈0)	2.499E-7 (≈0)	0.0823

Appendix C

Cross-sectional planes were used as references to measure the wall thickness and radius of curvature. The cross-sectional planes are shown in Fig. C1.

For each plane view, line segments can be constructed based on cross-sections of the surface geometry that also lie on the cross-sectional planes presented in Figure C.1 to make measurements for the radius of curvature. These line segments are highlighted on a Schwarz P unit cell as a representative example in Fig. C2. In creating line segments for the reconstructed unit cell model on the split plane, intersection points formed between lines originating from 3 adjacent pores are selected. This is graphically presented as yellow dots in the same aforementioned figure.

A midline within the enclosed line segments can be constructed before subsequently determining its length using Altair Hyperworks as shown in Fig. C3 By approximating the midline to take a circular arc, the arc angle, θ can be determined via ImageJ. The radius of curvature can subsequently be determined using the equation, $s = r\theta$, for s is the length of the midline/curvature. In regards to the wall thickness, the average length of the two ends of the enclosed line segments for each cross-sectional plane is tabulated. This should not be confused with the average wall thickness measured from unit cell micrographs at each plane view.

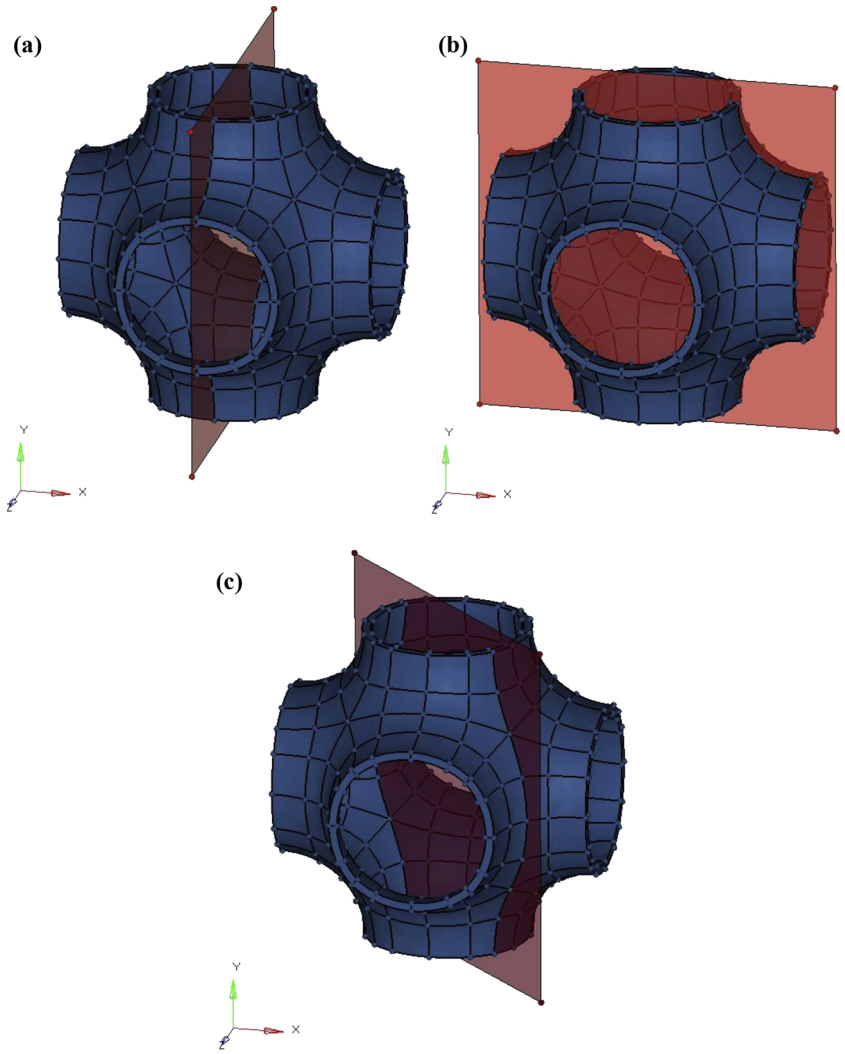

Fig. C1. Cross-sectional planes used as reference to measure the radius of curvature of reconstructed unit cells; (a) Plane YZ; (b) Plane YX; (c) Plane YX/YZ i.e. Split plane.

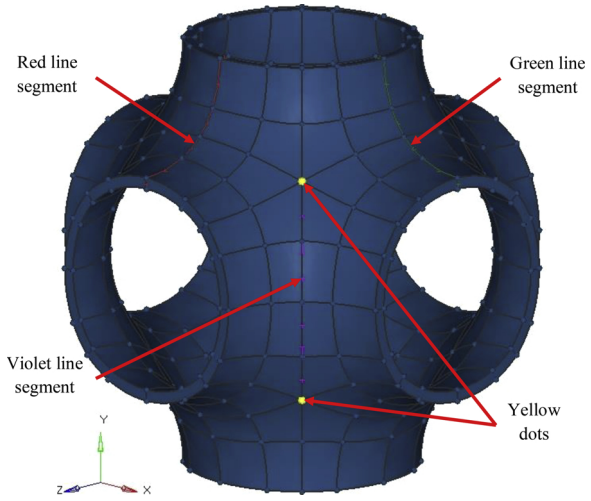

Fig. C2. Line segments on a Schwarz P unit cell. (Red) Line segment on the YZ plane; (Green) Line segment on the YX plane; (Violet) Line segment on the split plane; The line segment on the split plane is created between intersections points formed by line segments originating from 3 different adjacent pores. These intersections points are represented as yellow dots in the figure.

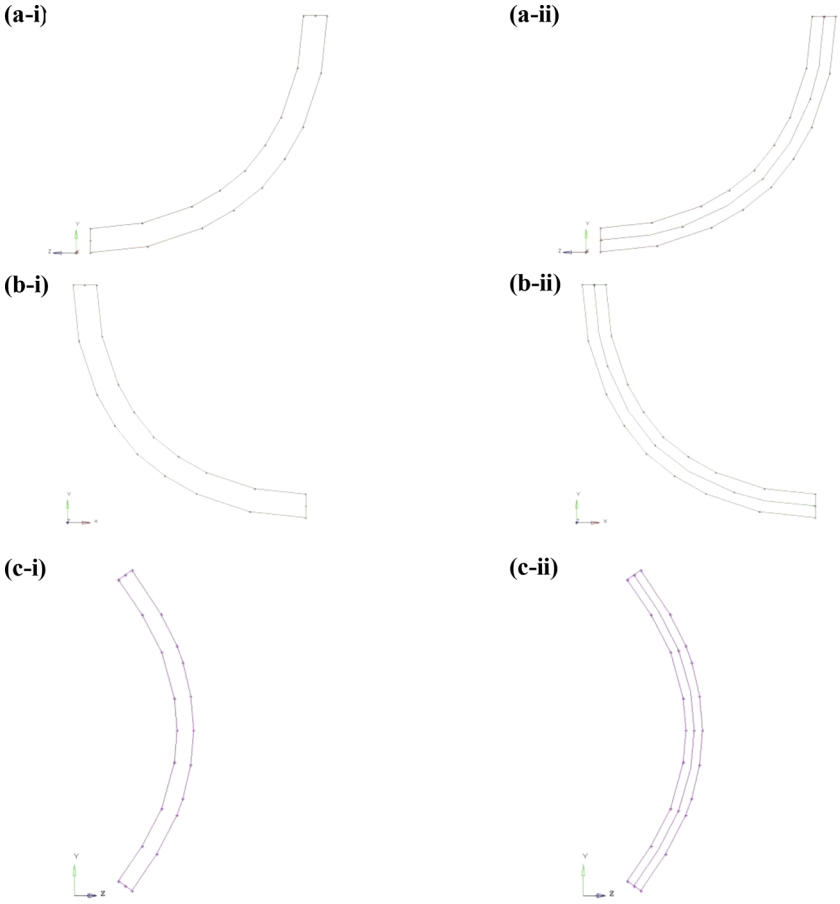

Fig. C3. Plane view of constructed line segments. (a–i) Line segment of cross-section at plane YZ; (a-ii) Construction of midline for line segment in a–i; (b–i) Line segment of cross-section at plane YX; (b-ii) Construction of midline for line segment in b–i; (c–i) Line segment of cross-section at the split plane; (c-ii) Construction of midline for line segment in.c–i.

Appendix D. Supplementary data

Supplementary material related to this article can be found, in the online version, at doi:https://doi.org/10.1016/j.addma.2018.11.021.

References

[1] W. Sun, B. Starly, J. Nam, A. Darling, Bio-CAD modeling and its applications in computer-aided tissue engineering, Bio-CAD 37 (2005) 1097–1114, https://doi.org/10.1016/j.cad.2005.02.002.
[2] D. Lacroix, J.A. Planell, P.J. Prendergast, Computer-aided design and finite-element modelling of biomaterial scaffolds for bone tissue engineering, Philos. Trans. A Math. Phys. Eng. Sci. 367 (2009) 1993–2009, https://doi.org/10.1098/rsta.2009.0024.
[3] E. Ramin, R.A. Harris, Advanced computer-aided design for bone tissue-engineering scaffolds, Proc. Inst. Mech. Eng. Part H J. Eng. Med. 223 (2009) 289–301, https://doi.org/10.1243/09544119JEIM452.
[4] X. Zhou, Y. Hou, J. Lin, A review on the processing accuracy of two-photon polymerization, AIP Adv. 5 (2015), https://doi.org/10.1063/1.4916886.
[5] F. Burmeister, S. Steenhusen, R. Houbertz, U.D. Zeitner, S. Nolte, A. Tünnermann, Materials and technologies for fabrication of three-dimensional microstructures with sub-100 nm feature sizes by two-photon polymerization, J. Laser Appl. 24 (2012) 42014, https://doi.org/10.2351/1.4730807.
[6] B. Tan, K. Venkatakrishnan, A. Makaronets, Effects of pulsewidth on two-photon polymerization, Des. Monomers Polym. 16 (2013) 145–150, https://doi.org/10.1080/15685551.2012.705502.
[7] R.J. Narayan, A. Doraiswamy, D.B. Chrisey, B.N. Chichkov, Medical prototyping using two photon polymerization, Mater. Today 13 (2010) 42–48, https://doi.org/10.1016/S1369-7021(10)70223-6.
[8] K. Sugioka, Y. Cheng, Femtosecond laser three-dimensional micro-and nanofabrication, Appl. Phys. Rev. 1 (2014), https://doi.org/10.1063/1.4904320.
[9] M. Malinauskas, V. Purlys, M. Rutkauskas, R. Gadonas, Two-photon polymerization for fabrication of three-dimensional micro- and nanostructures over a large area, in: 2009: 72040C–7204–11. https://doi.org/10.1117/12.811125.
[10] S. Sturm, S. Zhou, Y.-W. Mai, Q. Li, On stiffness of scaffolds for bone tissue engineering-a numerical study, J. Biomech. 43 (2010) 1738–1744, https://doi.org/10.1016/j.jbiomech.2010.02.020.
[11] S. Torquato, A. Donev, Minimal surfaces and multifunctionality, Proc. R. Soc. Lond. A Math. Phys. Eng. Sci. 460 (2004) 1849–1856, https://doi.org/10.1098/rspa.2003.1269.
[12] T. Femmer, A.J.C. Kuehne, M. Wessling, Estimation of the structure dependent performance of 3-D rapid prototyped membranes, Chem. Eng. J. 273 (2015) 438–445, https://doi.org/10.1016/j.cej.2015.03.029.
[13] B. Sahab, V. Nicolas, W. Pai, F.N.X.B. Katia, Harnessing deformation to switch on and off the propagation of sound, Adv. Mater. 28 (2015) 1631–1635, https://doi.org/10.1002/adma.201504469.
[14] N. Sreedhar, N. Thomas, O. Al-ketan, R. Rowshan, H.H. Hernandez, Mass transfer analysis of ultrafiltration using spacers based on triply periodic minimal surfaces: effects of spacer design, directionality and voidage, J. Membr. Sci. 561 (2018) 89–98, https://doi.org/10.1016/j.memsci.2018.05.028.
[15] O. Al-Ketan, M. Adel Assad, R.K. Abu Al-Rub, Mechanical properties of periodic interpenetrating phase composites with novel architected microstructures, Compos. Struct. 176 (2017) 9–19, https://doi.org/10.1016/j.compstruct.2017.05.026.
[16] S. Rajagopalan, R.A. Robb, Schwarz meets Schwann: design and fabrication of biomorphic and durataxic tissue engineering scaffolds, Med. Image Anal. 10 (2006) 693–712, https://doi.org/10.1016/j.media.2006.06.001.
[17] A.H. Schoen, Infinite periodic minimal surfaces without self-intersections, NASA Tech. (1997) Note D-5541.
[18] S.C. Kapfer, S.T. Hyde, K. Mecke, C.H. Arns, G.E. Schröder-Turk, Minimal surface scaffold designs for tissue engineering, Biomaterials 32 (2011) 6875–6882, https://doi.org/10.1016/j.biomaterials.2011.06.012.
[19] F.P.W. Melchels, K. Bertoldi, R. Gabbrielli, A.H. Velders, J. Feijen, D.W. Grijpma, Mathematically defined tissue engineering scaffold architectures prepared by stereolithography, Biomaterials 31 (2010) 6909–6916, https://doi.org/10.1016/j.biomaterials.2010.05.068.
[20] A. Ronca, L. Ambrosio, D.W. Grijpma, Preparation of designed poly(d,l-lactide)/nanosized hydroxyapatite composite structures by stereolithography, Acta Biomater. 9 (2013) 5989–5996, https://doi.org/10.1016/j.actbio.2012.12.004.
[21] R.M. Felfel, L. Poocza, M. Gimeno-Fabra, T. Milde, G. Hildebrand, I. Ahmed, C. Scotchford, V. Sottile, D.M. Grant, K. Liefeith, In vitro degradation and mechanical properties of PLA-PCL copolymer unit cell scaffolds generated by two-photon polymerization, Biomed. Mater. 11 (2016) 15011, https://doi.org/10.1088/1748-6041/11/1/015011.
[22] J. Shin, S. Kim, D. Jeong, H.G. Lee, D. Lee, J.Y. Lim, J. Kim, Finite element analysis

of schwarz P surface pore geometries for tissue-engineered scaffolds, Math. Probl. Eng. 2012 (2012) 13, https://doi.org/10.1155/2012/694194.
[23] Y. Jung, S. Torquato, Fluid permeabilities of triply periodic minimal surfaces, Phys. Rev. E 72 (2005) 56319, https://doi.org/10.1103/PhysRevE.72.056319.
[24] Z. Huang, Y. Nie, Z. Yang, Y. Li, N. Guo, Multiscale modeling for mechanical properties of cancellous bone based on the schwarz surface, MATEC Web Conf. 95 (2017) 12004, https://doi.org/10.1051/matecconf/20179512004.
[25] S. Li, A. Wongsto, Unit cells for micromechanical analyses of particle-reinforced composites, Mech. Mater. 36 (2004) 543–572, https://doi.org/10.1016/S0167-6636(03)00062-0.
[26] L. Musanje, J.L. Ferracane, R.L. Sakaguchi, Determination of the optimal photo-initiator concentration in dental composites based on essential material properties, Dent. Mater. 25 (2009) 994–1000, https://doi.org/10.1016/j.dental.2009.02.010.
[27] H.B. Sun, K. Takada, M.S. Kim, K.S. Lee, S. Kawata, Scaling laws of voxels in two-photon photopolymerization nanofabrication, Appl. Phys. Lett. 83 (2003) 1104–1106, https://doi.org/10.1063/1.1599968.
[28] A. Ovsianikov, X. Shizhou, M. Farsari, M. Vamvakaki, C. Fotakis, B.N. Chichkov, Shrinkage of microstructures produced by two-photon polymerization of Zr-based hybrid photosensitive materials, Opt. Express 17 (2009) 2143–2148.
[29] D. Karalekas, D. Rapti, E.E. Gdoutos, A. Aggelopoulos, Investigation of shrinkage-induced stresses in stereolithography photo-curable resins, Exp. Mech. 42 (2002) 439–444, https://doi.org/10.1007/BF02412150.
[30] T. Baldacchini, S. Snider, R. Zadoyan, Two-photon polymerization with variable repetition rate bursts of femtosecond laser pulses, Opt. Express 20 (2012) 29890–29899.
[31] D.-Y. Yang, S.H. Park, T.W. Lim, H.-J. Kong, S.W. Yi, H.K. Yang, K.-S. Lee, Ultraprecise microreproduction of a three-dimensional artistic sculpture by multi-path scanning method in two-photon photopolymerization, Appl. Phys. Lett. 90 (2007) 13113, https://doi.org/10.1063/1.2425022.
[32] H.-B. Sun, M. Maeda, K. Takada, J.W.M. Chon, M. Gu, S. Kawata, Experimental investigation of single voxels for laser nanofabrication via two-photon photo-polymerization, Appl. Phys. Lett. 83 (2003) 819–821, https://doi.org/10.1063/1.1598293.
[33] Y. Li, F. Qi, H. Yang, Q. Gong, X. Dong, X. Duan, Nonuniform shrinkage and stretching of polymerized nanostructures fabricated by two-photon photo-polymerization, Nanotechnology 19 (2008) 55303, https://doi.org/10.1088/0957-4484/19/05/055303.
[34] L. Poocza, M. Gottschaldt, E. Markweg, N. Hauptmann, G. Hildebrand, D. Pretzel, M. Hartlieb, C. Reichardt, J. Kübel, U.S. Schubert, O. Mollenhauer, B. Dietzek, K. Liefeith, Optimized photoinitiator for fast two-photon absorption polymerization of polyester-macromers for tissue engineering, Adv. Eng. Mater. 19 (2017), https://doi.org/10.1002/adem.201600686.
[35] J. Case, C.T.F. Ross, 18 Buckling of columns and beams 18.1, in: Strength Mater. Struct., 4th Editio, Butterworth-Heinemann, 1999: pp. 424–457.
[36] N.J. Sniadecki, Eccentric Loading (Lecture 33), Univ. Washingt., 2008.